2D MATERIALS

Electrical control of interlayer exciton dynamics in atomically thin heterostructures

Luis A. Jauregui[1]*, Andrew Y. Joe[1], Kateryna Pistunova[1], Dominik S. Wild[1], Alexander A. High[1,2], You Zhou[1,2], Giovanni Scuri[1], Kristiaan De Greve[1,2]†, Andrey Sushko[1], Che-Hang Yu[3]‡, Takashi Taniguchi[4], Kenji Watanabe[4], Daniel J. Needleman[3,5,6], Mikhail D. Lukin[1], Hongkun Park[1,2], Philip Kim[1,3]§

A van der Waals heterostructure built from atomically thin semiconducting transition metal dichalcogenides (TMDs) enables the formation of excitons from electrons and holes in distinct layers, producing interlayer excitons with large binding energy and a long lifetime. By employing heterostructures of monolayer TMDs, we realize optical and electrical generation of long-lived neutral and charged interlayer excitons. We demonstrate that neutral interlayer excitons can propagate across the entire sample and that their propagation can be controlled by excitation power and gate electrodes. We also use devices with ohmic contacts to facilitate the drift motion of charged interlayer excitons. The electrical generation and control of excitons provide a route for achieving quantum manipulation of bosonic composite particles with complete electrical tunability.

Long-lived excitons can be potentially used for the realization of coherent quantum many-body systems (*1*–*3*) or as quantum information carriers (*4*, *5*). In conventional semiconductors, the exciton lifetime can be increased by constructing double–quantum well (DQW) heterostructures, in which spatially separated electrons and holes form interlayer excitons (IEs) across the quantum wells (*6*–*12*). Strongly bound IEs can also be formed by stacking two single atomic unit cells of transition metal dichalcogenides (TMDs) into a van der Waals (vdW) heterostructure. TMD heterostructures, such as $MoSe_2/WSe_2$, MoS_2/WS_2, and MoS_2/WSe_2, have shown ultrafast charge transfer (*13*), the formation of IEs with a large binding energy of ~150 meV (*14*), and diffusion over long distances (*15*). Moreover, the tight binding and small exciton Bohr radius potentially allow for quantum degeneracy of these composite bosons, which may lead to exciton condensation at substantially elevated temperatures compared to those of, e.g., conventional Bose-Einstein condensates of cold atoms (*2*).

In this work, we fabricate individually electrically contacted optoelectronic devices using hexagonal boron nitride (h-BN)–encapsulated vdW heterostructures of $MoSe_2$ and WSe_2 (*16*, *17*). Optically transparent electrical gates and ohmic electrical contacts realized for the individual atomic layers allow us to have complete control of the carrier densities in each TMD of the DQW while maintaining full optical access. The top and bottom insets of Fig. 1A show an optical image of a representative device with false-colored top gates and a schematic cross section, respectively [a detailed device scheme is illustrated in fig. S1 (*18*)]. The green and red false-colored gates depict the contact gates for doping the $MoSe_2$ and WSe_2 regions, respectively. These contact gates, together with the prefabricated Pt electrodes, provide ohmic contacts in the WSe_2 p-channel (*19*).

The presence of the top (optically transparent) and bottom electrical gates, in addition to the separately contacted TMD layers, allows us to control the carrier density in the individual TMD layers as well as the electric field across the TMD heterostructure, E_{hs}, using the voltage V_{tg} (or V_{bg}) applied to the top (or bottom) gate. For intrinsic TMD layers (i.e., no free carriers and the chemical potential located within the semiconducting gap), where the heterostructure can be approximated by a thin dielectric slab, E_{hs} is controlled by a gate operation scheme in which we apply opposite gate polarity [supplementary text section 1 in (*18*)]. Figure 1A shows the photoluminescence (PL) spectrum measured at temperature $T = 4$ K as a function of E_{hs}, keeping both TMD layers intrinsic. We observe a linear shift of PL peak energy with E_{hs}, suggesting a first-order Stark shift caused by the static electric dipole moment across the vdW heterostructure. By fitting the linear PL peak shift with the linear Stark shift formula $-edE_{hs}$, where ed is the dipole moment (e, electron charge; d, electron–hole separation), we estimate $d \approx 0.6$ nm, in good agreement with the expected vdW separation between WSe_2 and $MoSe_2$. This analysis strongly suggests that the observed PL peak indeed corresponds to the IE emission of the $WSe_2/MoSe_2$ heterostructure with out-of-plane–oriented electric dipoles. There is a ~10% nonlinearity in the energy shift dependence versus E_{hs}, which, combined with weak variations of the absorption intensity (as shown in Fig. 1B), might be attributed to the charging effect caused by uncompensated gating. Similar to a previous study (*14*), our findings indicate that the PL from the intralayer excitons is strongly suppressed compared with that of IEs in the $WSe_2/MoSe_2$ heterostructure region [fig. S2 in (*18*)], suggesting a fast dissociation of intralayer excitons and an efficient conversion to IEs in this system. We further confirm from the constant normalized reflection $\Delta R/R$ at the intralayer exciton resonances (*20*–*22*) that our gate operation scheme only varies E_{hs} while keeping the layers intrinsic (Fig. 1B).

The IEs in the vdW heterostructure can live longer than intralayer excitons, owing to the spatial separation of electrons and holes in the heterostructure. Figure 1C shows the IE lifetime τ as a function of E_{hs}, measured by time-dependent PL after pulsed laser illumination. The lifetime τ increases as E_{hs} increases, reaching ≈600 ns for $E_{hs} > 0.1$ V/nm, an order of magnitude larger than in previous studies (*14*, *23*). The observed dependence of τ on E_{hs} can be explained by changes in the overlap between the electron and hole wave functions [section 3 of (*18*)]. The recombination rate of an exciton is proportional to the probability that the electron and the hole occupy the same location. An electric field antiparallel to the IE dipole moment is therefore expected to reduce the recombination rate as it pulls the two carriers apart, consistent with our measurements. Considering the PL intensity modulation shown in Fig. 1A together with the measured τ, we also demonstrate that the emission efficiency (η) can be tuned with E_{hs}, reaching η ~ 80% when E_{hs} is aligned against the IE dipole moment, promoting the recombination process [section 4 of (*18*)].

The electrostatic condition in our heterostructures is greatly modified if we change the gate operation scheme such that one of the TMD layers is doped electrostatically, introducing free charge carriers. Figure 1E shows the IE PL spectrum after the gating scheme depicted in Fig. 1D. In this scheme, as shown in the normalized reflection $\Delta R/R$ at the intralayer exciton resonances (Fig. 1F), the carrier density of $MoSe_2$ (WSe_2), n_{2D} (p_{2D}), changes with positive V_{tg} (negative V_{bg}) while the WSe_2 ($MoSe_2$) layer remains intrinsic, keeping E_{hs} constant [section 5 of (*18*)]. We observe several pronounced changes in the IE emission spectrum as V_{tg} (V_{bg}) increases (decreases) and $n_{2D} > 0$ ($p_{2D} > 0$). First, the IE PL peaks exhibit a sudden red shift for n-doping (p-doping) of $MoSe_2$

[1]Department of Physics, Harvard University, Cambridge, MA, USA. [2]Department of Chemistry and Chemical Biology, Harvard University, Cambridge, MA, USA. [3]John A. Paulson School of Engineering and Applied Sciences, Harvard University, Cambridge, MA, USA. [4]National Institute for Materials Science, 1-1 Namiki, Tsukuba, Japan. [5]Department of Molecular and Cellular Biology, Harvard University, Cambridge, MA, USA. [6]Faculty of Arts and Sciences Center for Systems Biology, Harvard University, Cambridge, MA, USA.
*Present address: Department of Physics and Astronomy, University of California, Irvine, CA, USA. †Present address: Imec, Leuven, Belgium. ‡Present address: Department of Electrical and Computer Engineering, University of California, Santa Barbara, CA, USA.
§Corresponding author. Email: pkim@physics.harvard.edu

(WSe_2). Second, the PL peaks continuously redshift as doping increases for both n- and p-sides. In this regime, E_{hs} is fixed (as discussed above) and thus these shifts cannot be explained by the Stark effect. Lastly, the PL intensity diminishes rapidly as doping increases.

Our measurements in the doped regime can be explained by the formation of charged IEs (CIEs) (*24*). As shown in the normalized reflection measured with the same gating scheme, we can identify (i) intrinsic/p, (ii) intrinsic/intrinsic, and (iii) n/intrinsic regions by the disappearance of the absorption dips for intralayer excitons in $MoSe_2$ and WSe_2 (*25*), which are well aligned with the sudden red shift observed in IE PL (vertical dashed lines in Fig. 1, D to G). Thus, this jump in energy can be related to the CIEs. Note that charged excitons can be referred to as trions (i.e., three-body bound states) (*26*–*29*) or, alternatively, attractive polarons (i.e., excitonic states dressed by a polarized fermionic sea, similar to those in monolayer TMDs) (*30*, *31*). The value of the observed jump ≈10 meV (15 meV) for positive (negative) CIEs is in good agreement with the calculated binding energy of CIEs (*24*). The lifetime of CIEs is ≈100 ns near the band edge but decreases with increased doping, presumably owing to additional decay channels enabled by scattering with free carriers (Fig. 1G).

We create high densities of IEs by increasing laser power. In particular, for neutral IEs, we observe that the PL emission is shifted to higher energy with increasing power (Fig. 2A), consistent with a mean-field shift stemming from the repulsive dipole–dipole interaction between oriented IEs. Following the analysis based on a parallel plate-capacitance model used for GaAs DQW IEs (*32*), we obtain a lower bound for the IE density of ~5×10^{11} cm^{-2} [section 6 of (*18*)]. The high density of long-lived IEs and the large τ observed in our heterostructures can enable transport of IEs across the samples. Figure 2, B to D, shows the spatial map of the IE PL intensity at different laser powers. The PL signal can be detected far away from the diffraction-limited focused laser spot (<1 μm in diameter). At the highest power, PL can be observed many micrometers away from the excitation spot, strongly suggesting transport of IEs across the sample. From these maps, we obtain the normalized, radially averaged PL intensity, $I_{PL}^{norm}(r)$, where r is measured from the center of the diffraction-limited steady-state laser spot. Here, the PL intensity is normalized by the value obtained at r = 0. As shown in Fig. 2E, away from the laser spot, $I_{PL}^{norm}(r)$ decreases rapidly as r increases. Note, however, that at a given r, $I_{PL}^{norm}(r)$ increases with power (P) even at a position far away from the laser spot. Similarly, an increase of $I_{PL}^{norm}(r)$ is observed when adjusting E_{hs} to increase τ at fixed P. The latter observation is consistent with exciton transport, as longer-lived IEs may travel farther [section 7 of (*18*)]. The characteristic length L_D for the decaying behavior of $I_{PL}^{norm}(r)$ can

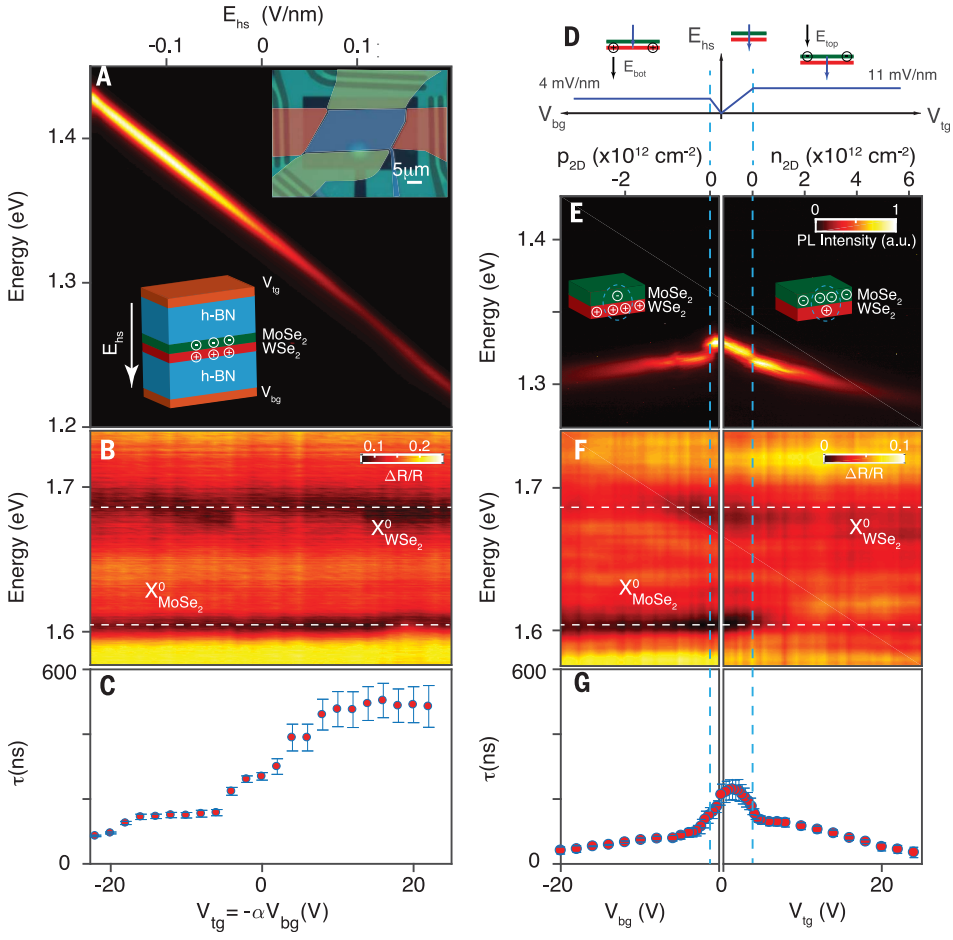

Fig. 1. Electric field and carrier density control of interlayer excitons. (**A**) IE PL spectra versus electric field applied to the heterostructure [$E_{hs} = (V_{tg} - V_{bg})/t_{total} * (\varepsilon_{h-BN}/\varepsilon_{TMD})$]. Here, the top ($V_{tg}$) and bottom ($V_{bg}$) gate voltages are swept together with a voltage ratio α ($\alpha = t_{top}^{h-BN}/t_{bottom}^{h-BN} = 0.614$; $t_{top}^{h-BN} = 70$nm and $t_{bottom}^{h-BN} = 114$nm are the top and bottom h-BN thicknesses, respectively), t_{total} is the total h-BN thickness, and $\varepsilon_{h-BN} = 3.9$ and $\varepsilon_{TMD} = 7.2$ are the h-BN and TMD permittivity, respectively. (Top inset) Optical image of a representative device with the top-gates shown in false color. (Bottom inset) Schematic of the heterostructure cross section, showing electrons (holes) accumulate on the $MoSe_2$ (WSe_2) layers, forming IEs. The white arrow represents the positive direction of E_{hs}. (**B**) Normalized reflectance versus E_{hs}. (**C**) IE lifetime τ versus E_{hs}. The lifetime is measured at low laser power (20 nW) to ensure a single exponential PL decay. Error bars are obtained by adjusting the fitting range. (**D**) Calculated E_{hs} versus V_{tg} and V_{bg}. The field E_{hs} remains constant once a given layer is doped. The top cartoons represent the heterostructure for different applied gate voltages. The fields E_{hs} and E_{BN} (electric fields on the top and bottom h-BN layers) are depicted as blue and black arrows, respectively. (**E**) Single-gate dependence (V_{tg} or V_{bg}) of the PL shows formation of charged IEs with varying carrier density obtained from the gate operation scheme in (D). (Left inset) Cartoon of hole-doped IEs with V_{bg}. (Right inset) Cartoon of electron-doped IEs with V_{tg}. a.u., arbitrary units. (**F**) Normalized reflectance versus carrier density. The horizontal dashed lines in (B) and (F) represent the neutral excitons for WSe_2 ($X^0_{WSe_2}$) and $MoSe_2$ ($X^0_{MoSe_2}$). The normalized reflection spectrum from the top $MoSe_2$ layer is brighter than that from the bottom WSe_2 layer, owing to the dominant direct reflection of the top layer, which provides a simpler normalization scheme. (**G**) Neutral and charged IE lifetimes τ versus carrier density. Error bars are obtained by adjusting the fitting range. The vertical light blue dashed lines in (D) to (G) mark the intrinsic region. Data in (E) to (G) were taken in different thermal cycles from (A) to (C). Thus, small shifts in the energy spectrum or lifetime occur, owing to different disorder configurations and measurement positions at low temperatures.

be obtained from fitting $e^{-r/L_D}/\sqrt{r/L_D}$ to $I_{PL}^{norm}(r)$ away from the laser excitation spot (dashed lines in Fig. 2E), following the two-dimensional diffusion model with a point source [section 8 in (*18*)]. As shown on the left axis of Fig. 2G, we find that L_D increases as P increases, suggesting increased diffusion at high IE density, possibly due to exciton–exciton interactions.

We also used a diffraction-limited focused pulsed laser to measure the temporal decay of the PL intensity. Figure 2F shows an estimate of the time-dependent exciton population (integrated PL signal along the heterostructure weighted by r^2) after a laser pulse with peak power P. The time-dependent PL initially exhibits a faster decay process with characteristic time scale $\tau_1 \sim 10$ ns, followed by a slower decay process occurring on the time scale $\tau_2 \sim 100$ ns, suggesting that there are two different mechanisms for the PL intensity decay. The value of L_D estimated above can be converted to a diffusion constant according to $D = L_D^2/\tau$. Two values D_1 and D_2 are obtained using the short (τ_1) and long (τ_2) decay times, respectively (Fig. 2H). Because our lifetime measurement uses a pulsed laser where the interaction-driven IE diffusion occurs just after the pulse is off when the IE density remains high, τ_1 could be more relevant than τ_2 for the IE diffusion. However, the value of L_D, measured in steady state, would be dominated by τ_2. Figure 2H shows that D_2 is in the range of 0.01 to 0.1 cm^2/s, whereas D_1 changes from 0.1 to 1 cm^2/s. Both D_1 and D_2 are increasing with increasing P, providing upper and lower bounds for nonlinear IE diffusion caused by dipolar repulsive interaction [section 8 in (*18*)], respectively.

We obtain further evidence for IE transport from time-dependent spatial PL maps with a pulsed laser illuminating the center of the sample. We measure the IE PL intensity $I_{PL}(r, t)$ as a function of distance r (referenced to the laser illumination spot) and time t (referenced to the falling edge of the laser pulse). Figure 2, I

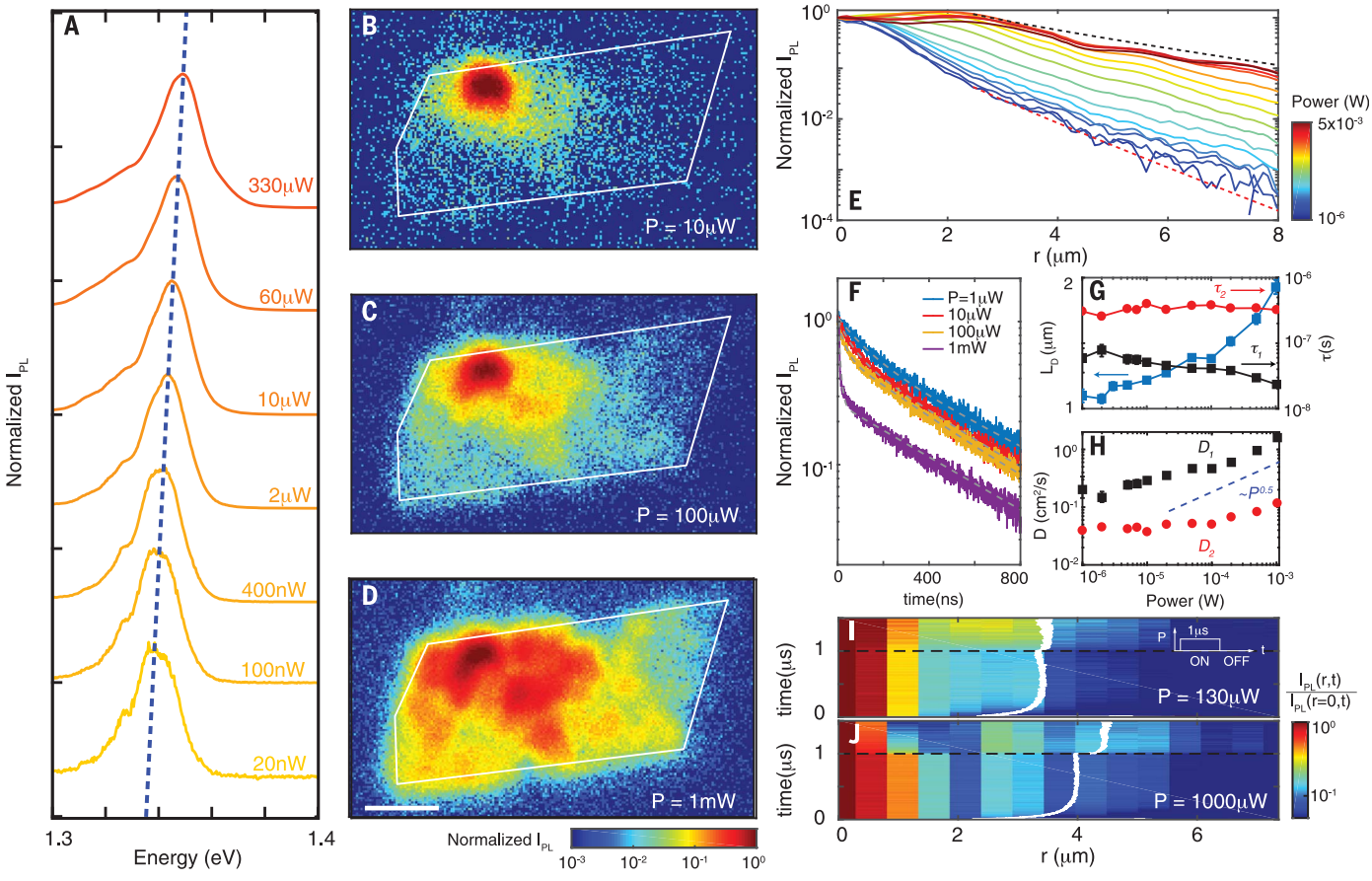

Fig. 2. Spatial control of neutral interlayer excitons. (**A**) Power (P) dependence of the normalized PL spectra collected from the same spot as the excitation. The blue dashed line corresponds to the PL peak position versus power. (**B** to **D**) Spatial dependence of the intensity of the normalized PL for P = 10, 100, and 1000 μW, respectively. The white outlines depict the heterostructure area. The continuous wave laser excitation (λ = 660 nm) is fixed at the top left of the sample. Scale bar, 5 μm. All measurements were performed at 4 K. Experiments performed at higher temperatures provide smaller spatial extension of PL around the excitation [see section 12 of (*18*) for details]. (**E**) Power dependence of normalized radially averaged I_{PL} (normalized I_{PL}) versus r with the excitation fixed at the center of the sample. The red and black dashed lines represent $e^{-r/L_D}/\sqrt{r/L_D}$ for L_D = 1.1 and 3.2 μm, respectively, where L_D is the diffusion length. P = 1, 2, 3, 5, 10, 20, 50, 100, 200, 500, 1000, 2000, 3000, 4000, and 5000 μW. (**F**) Time-dependent PL normalized at t = 0 for different "on" powers. For this measurement, we use a pulsed 660-nm diode laser with a 100-kHz repetition rate and 1-μs "on" time. The power we quoted is the "on" power or peak power. Dashed gray lines correspond to double exponential fits. (**G**) (Left axis) L_D versus P extracted from the data in (E). (Right axis) Lifetime (τ) versus P with two values of τ extracted from the double exponential decay fit. (**H**) Diffusion constant ($D = L_D^2/\tau$) versus P extracted from (G) using the two different values of τ. The dashed line corresponds to $D \sim P^{1/2}$, as expected from the nonlinear diffusion model [section 8 of (*18*)]. (**I** and **J**) Normalized I_{PL} versus time and distance from the laser spot. $I_{PL}(r, t)$ was estimated by averaging over a line cut through the laser spot. We normalize I_{PL} at each time by $I_{PL}(r, t)/I_{PL}(r = 0, t)$. Overlaid white lines represent $\sqrt{\langle r^2 \rangle}$ obtained from the experimental PL map, assuming rotational symmetry of the sample. (Inset) The pulsed laser diode is turned on at t = 0 μs with powers of 130 μW (I) and 1000 μW (J) and turned off at t = 1 μs (also marked with dashed black lines).

and J, shows the normalized time-dependent PL $I_{PL}^{norm}(r,t) = I_{PL}(r,t)/I_{PL}\ (r=0,t)$ at different laser peak powers. The time-dependent root mean square radius, $r_{rms}(t) = \sqrt{\langle r^2 \rangle}$, computed from $I_{PL}^{norm}(r,t)$ (white lines) increases rapidly when the laser is on, reaching a steady state within ~200 ns. Notably, $r_{rms}(t)$ increases again rapidly within 100 ns after the laser is turned off. Although the observed two decaying time scales and the dynamics of IEs can be explained by the diffusion of IEs driven by interaction and their recombination, an alternative scenario involving the diffusion of photoexcited free carriers (*33*) is also possible [see section 8 of (*18*)]. Future experimental studies with spatially resolved resonant excitation of IEs can be potentially used to distinguish these scenarios.

Unlike the neutral IEs discussed above, CIEs can be manipulated by an in-plane electric field. Figure 3A shows the spatial map of I_{PL} overlaid with the device image when CIEs are optically excited at the center of the sample. Similar to neutral IEs, CIEs generated at the laser-illuminated spot can diffuse across the entire sample. Both the WSe_2 and $MoSe_2$ layers in our device have multiple electrical contacts away from the heterostructure edge (~10 μm away) that are used to control the lateral electric field while avoiding any local Schottky barrier effects. Figure 3B shows the spatial map of the PL intensity normalized as $I_{PL}(V_{ds})/I_{PL}(V_{ds} = 0)$ when applying an interlayer bias voltage of V_{ds} = 3 V across the WSe_2 layer. We observe that the grounded edge of the sample becomes brighter with increasing V_{ds} (also see Fig. 3C for the normalized average emission intensity along the heterostructure channel). This increase in PL at the boundary between the heterostructure and the highly doped monolayer region can be explained by drift of CIEs under the applied bias voltage in the channel. The applied bias V_{ds} creates an electric field to tilt the band structure in the direction of the WSe_2 channel, driving positive (+) CIEs along the same direction as shown in the schematic diagram in Fig. 3D. At the boundary of the heterostructure, however, the +CIE cannot be transported to the WSe_2 p-channel because current across the boundary must be preserved. Therefore, the transported +CIEs recombine to turn into a hole in the WSe_2 p-channel. In figs. S13 and S14, we further confirm this picture of CIE transport by changing the doping polarity and V_{ds} direction [see section 9 of (*18*) for details on gate configurations and alternative explanations]. We also note that, owing mainly to the limited resolution of our electrical setup, we do not observe any photocurrent >10 pA.

Finally, we demonstrate the electrical generation of IEs by free-carrier injection using ohmic contacts in individual TMD layers. Because our heterostructure forms type II–aligned p- and n-layers, the charge transport across WSe_2 to $MoSe_2$ is expected to show diode-like rectifying behaviors (*34*, *35*). Figure 4A shows interlayer current (I_{ds}) versus interlayer bias (V_{ds}) curves, whose characteristics can be modulated by V_{tg} and V_{bg}. Changing V_{tg} and V_{bg} adjusts the band offset in the type II heterojunction and the doping in each layer. The inset to Fig. 4A shows a map of the forward bias current at a fixed bias voltage. One can identify the region in which both WSe_2 and $MoSe_2$ layers remain intrinsic, consistent with the absorption spectrum discussed in Fig. 1. Notably, we find that this p-n device generates detectable electroluminescence (EL) at sufficiently high bias. A particularly interesting EL condition occurs when both TMD layers are intrinsic, thus allowing electrons and holes to

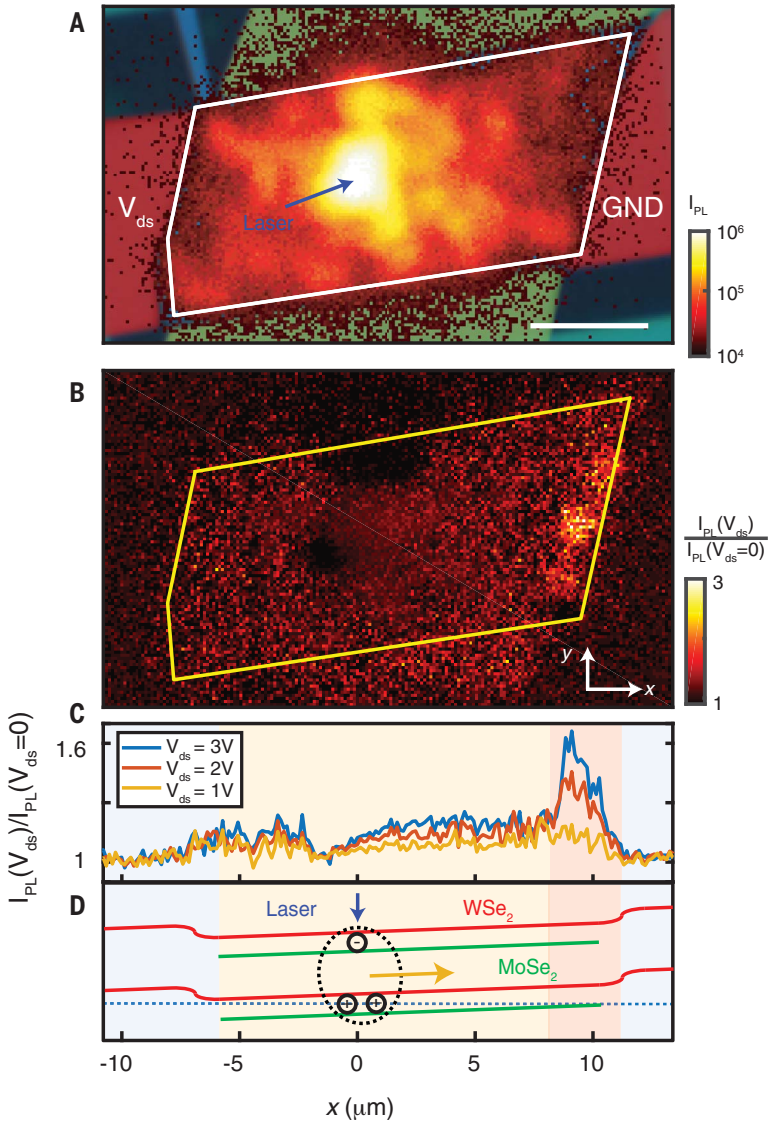

Fig. 3. Spatial control of charged interlayer excitons. (**A**) Spatial dependence of I_{PL} with the laser excitation fixed at the center of the heterostructure (blue arrow). An optical image of the device with false-colored top gates that cover the WSe_2 and $MoSe_2$ contacts is overlaid. An in-plane electric field is applied by a voltage (V_{ds}) in one of the WSe_2 contacts while the other contact remains grounded. GND corresponds to the grounded electrode. Scale bar, 5 μm. (**B**) Spatial dependence of I_{PL} normalized according to $I_{PL}(V_{ds})/I_{PL}(V_{ds} = 0)$ for V_{ds} = 3 V. When V_{ds} increases, we observe a larger population of charged IEs near the right WSe_2 electrode. (**C**) Normalized I_{PL} averaged over the *y* axis versus the heterostructure channel length *x* [depicted in (B)] for different V_{ds}. (**D**) Schematic of the heterostructure bands with applied V_{ds}. The red (green) bands correspond to WSe_2 ($MoSe_2$). A positive V_{ds} is applied while the chemical potential (blue dotted line) is kept inside the WSe_2 valence band to form positively charged IEs. Under positive V_{ds}, the CIEs drift toward the grounded contact. The emission mainly occurs near the grounded contact, because the charged exciton cannot move beyond the heterostructure. The yellow arrow indicates the current direction.

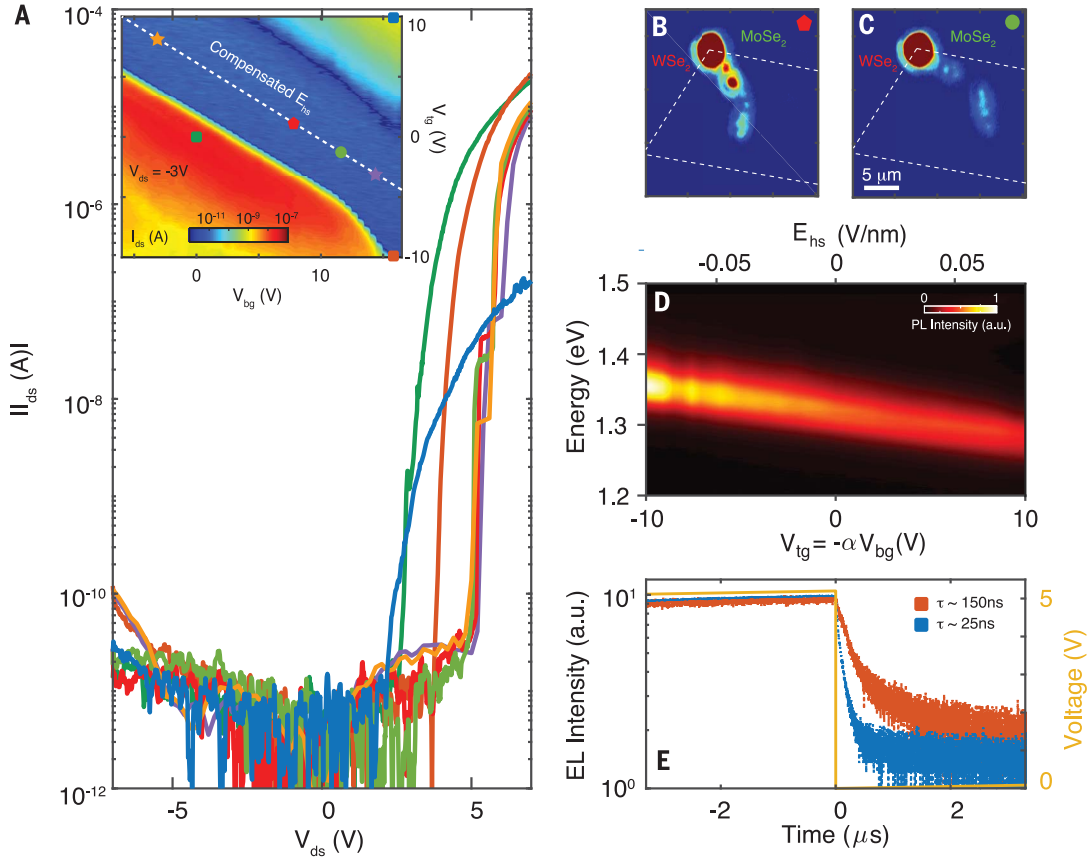

Fig. 4. Electrical generation of interlayer excitons. (**A**) *I-V* curves at various top (V_{tg}) and bottom (V_{bg}) gate configurations, with corresponding indicators in the inset. (Inset) I_{ds} versus V_{tg} and V_{bg} (with V_{ds} = −3 V on $MoSe_2$ and grounded WSe_2). The white dashed line represents the compensated electric field where $V_{bg} = 10.37V - \alpha V_{tg}$. The different symbols represent the gate voltages used in (A) to (C) and (E). (**B** and **C**) Spatially dependent EL maps for V_{tg} = −1 V (1 V) and V_{bg} = 12 V (8.75 V) at V_{ds} = 7 V. The white dashed lines indicate the heterostructure area. (**D**) Electric field (E_{hs}) dependence of the interlayer exciton EL. The electron–hole separation ($d \approx 0.55$ nm) obtained from the slope agrees reasonably with the electron–hole separation extracted from PL. (**E**) Time-dependent EL intensity for two different gate configurations: blue (orange) curve uses V_{tg} = 10 V (−10 V) and V_{bg} = 16.28 V. The yellow line represents the pulsed sawtooth voltage applied to V_{ds}. The measured EL lifetime is gate-tunable, as in the PL case, and of comparable magnitude to the PL lifetime.

recombine through the formation of IEs. Figure 4, B and C, shows the EL maps of the heterostructure region. The local EL intensity in the heterostructure depends on the local recombination current density, which can be controlled by V_{tg} and V_{bg} [section 10 of (*18*)]. We find that the EL spectrum resembles the PL spectrum in the same (V_{tg}, V_{bg}) configuration (*34*). Figure 4D shows EL versus E_{hs}. Similar to the PL shown in Fig. 1A, the EL spectrum shifts linearly with E_{hs}, which can be attributed to the IE Stark effect. More direct evidence that the EL process in our heterostructure is mediated through the IE formation by carrier injection is provided by the EL lifetime. Figure 4E shows the EL intensity as a function of time when we pulse V_{ds} at a fixed V_{tg} and V_{bg}. We measure the EL at the falling edge of the pulse. Long and short lifetimes of ≈150 and ≈25 ns are obtained for the gate voltages of V_{tg} = 10 and −10 V with V_{bg} = 16.3 V, corresponding to the neutral IE and charged IE formation regime, respectively (Fig. 4A, inset).

The electrical generation of long-lived interlayer excitons provides an electrically driven near-infrared light source with an energy tunability that ranges over several hundreds of milli–electron volts and spatial control of the emission. Achieving high-density IEs without optical excitation could pave a way to realize quantum condensates in solid-state devices. Large valley polarization (*23*, *36*) strongly coupled to the spin may also lead to optoelectronic devices based on electrically driven CIEs. The spin degree of freedom in such devices could be potentially used for both classical and quantum information processing.

REFERENCES AND NOTES

1. L. V. Butov *et al.*, *Phys. Rev. Lett.* **86**, 5608–5611 (2001).
2. M. M. Fogler, L. V. Butov, K. S. Novoselov, *Nat. Commun.* **5**, 4555 (2014).
3. M. Combescot, R. Combescot, F. Dubin, *Rep. Prog. Phys.* **80**, 066501 (2017).
4. I. Schwartz *et al.*, *Science* **354**, 434–437 (2016).
5. E. Poem *et al.*, *Nat. Phys.* **6**, 993–997 (2010).
6. A. A. High *et al.*, *Nano Lett.* **12**, 2605–2609 (2012).
7. A. A. High *et al.*, *Nature* **483**, 584–588 (2012).
8. A. A. High *et al.*, *Phys. Rev. Lett.* **103**, 087403 (2009).
9. A. A. High *et al.*, *Nano Lett.* **9**, 2094–2098 (2009).
10. A. T. Hammack *et al.*, *Phys. Rev. Lett.* **96**, 227402 (2006).
11. L. V. Butov, C. W. Lai, A. L. Ivanov, A. C. Gossard, D. S. Chemla, *Nature* **417**, 47–52 (2002).
12. R. Rapaport *et al.*, *Phys. Rev. Lett.* **92**, 117405 (2004).
13. X. Hong *et al.*, *Nat. Nanotechnol.* **9**, 682–686 (2014).
14. P. Rivera *et al.*, *Nat. Commun.* **6**, 6242 (2015).
15. D. Unuchek *et al.*, *Nature* **560**, 340–344 (2018).
16. X. M. Liu, K. Watanabe, T. Taniguchi, B. I. Halperin, P. Kim, *Nat. Phys.* **13**, 746–750 (2017).
17. L. Wang *et al.*, *Science* **342**, 614–617 (2013).
18. See supplementary materials.
19. B. Fallahazad *et al.*, *Phys. Rev. Lett.* **116**, 086601 (2016).
20. G. Scuri *et al.*, *Phys. Rev. Lett.* **120**, 037402 (2018).
21. Y. Zhou *et al.*, *Nat. Nanotechnol.* **12**, 856–860 (2017).
22. Z. Wang, L. Zhao, K. F. Mak, J. Shan, *Nano Lett.* **17**, 740–746 (2017).
23. P. Rivera *et al.*, *Science* **351**, 688–691 (2016).
24. I. V. Bondarev, M. R. Vladimirova, *Phys. Rev. B* **97**, 165419 (2018).
25. A. M. Jones *et al.*, *Nat. Nanotechnol.* **8**, 634–638 (2013).
26. J. S. Ross *et al.*, *Nat. Commun.* **4**, 1474 (2013).
27. G. Finkelstein, H. Shtrikman, I. Bar-Joseph, *Phys. Rev. B* **53**, R1709–R1712 (1996).
28. K. Kheng *et al.*, *Phys. Rev. Lett.* **71**, 1752–1755 (1993).
29. M. A. Lampert, *Phys. Rev. Lett.* **1**, 450–453 (1958).
30. M. Sidler *et al.*, *Nat. Phys.* **13**, 255–261 (2017).
31. R. Schmidt, T. Enss, V. Pietila, E. Demler, *Phys. Rev. A* **85**, 021602 (2012).
32. B. Laikhtman, R. Rapaport, *Phys. Rev. B* **80**, 195313 (2009).
33. L. V. Butov *et al.*, *Phys. Rev. Lett.* **92**, 117404 (2004).
34. J. S. Ross *et al.*, *Nano Lett.* **17**, 638–643 (2017).
35. C. H. Lee *et al.*, *Nat. Nanotechnol.* **9**, 676–681 (2014).
36. X. D. Xu, W. Yao, D. Xiao, T. F. Heinz, *Nat. Phys.* **10**, 343–350 (2014).
37. L. Jauregui, Replication data for: Electrical control of interlayer exciton dynamics in atomically thin heterostructures. Harvard Dataverse (2019); https://doi.org/10.7910/DVN/IZQAVH.

ACKNOWLEDGMENTS

We thank E. Demler, S. Fang, and F. Pientka for discussions. **Funding:** This work is supported by the DoD Vannevar Bush Faculty Fellowship (N00014-18-1-2877 for P.K., N00014-16-1-2825 for H.P.), AFOSR MURI (FA9550-17-1-0002), NSF and CUA (PHY-1506284 and PHY-1125846 for H.P. and M.D.L.), ARL (W911NF1520067 for H.P. and M.D.L.), the Gordon and Betty Moore Foundation (GBMF4543 for P.K.), and Samsung Electronics (for P.K. and H.P.). This work was performed in part at the Center for Nanoscale Systems (CNS), a member of the National Nanotechnology Coordinated Infrastructure (NNCI), which is supported by the National Science Foundation under NSF award 1541959. CNS is part of Harvard University. D.J.N. acknowledges

support from the NSF grant DBI-0959721. A.S. acknowledges support from the Fannie and John Hertz Foundation and the Paul & Daisy Soros Fellowships for New Americans. K.W. and T.T. acknowledge support from the Elemental Strategy Initiative conducted by the MEXT, Japan, and the CREST (JPMJCR15F3), JST. **Author contributions:** L.A.J., A.Y.J., and P.K. conceived the project. L.A.J., A.Y.J., K.P., A.A.H., Y.Z., G.S., K.D.G., and A.S. designed and performed the experiments. L.A.J., A.Y.J., and K.P. fabricated the devices and analyzed the data. L.A.J., A.Y.J., K.P., D.S.W., and P.K. wrote the manuscript with the help of all authors. D.S.W. developed the theoretical model. T.T. and K.W. grew the h-BN crystals. C.-H.Y. and D.J.N. developed the second harmonic generation setup, which was used to align the individual flakes. M.D.L., H.P., and P.K. supervised the project. **Competing interests:** The authors declare no competing interests. **Data and materials availability:** All data needed to evaluate the conclusions in the paper are present in the paper or the supplementary materials and have been deposited at the Harvard Dataverse (*37*).

SUPPLEMENTARY MATERIALS

science.sciencemag.org/content/366/6467/870/suppl/DC1
Materials and Methods
Supplementary Text
Figs. S1 to S18
References (*38*–*45*)

19 December 2018; accepted 18 October 2019
10.1126/science.aaw4194

Science

Electrical control of interlayer exciton dynamics in atomically thin heterostructures

Luis A. Jauregui, Andrew Y. Joe, Kateryna Pistunova, Dominik S. Wild, Alexander A. High, You Zhou, Giovanni Scuri, Kristiaan De Greve, Andrey Sushko, Che-Hang Yu, Takashi Taniguchi, Kenji Watanabe, Daniel J. Needleman, Mikhail D. Lukin, Hongkun Park and Philip Kim

Science **366** (6467), 870-875.
DOI: 10.1126/science.aaw4194

Taking electrical control

Excitons—bound pairs of electrons and holes in a solid—can, in principle, be used as information carriers. However, their lifetime is limited because the electrons and holes tend to quickly recombine. One way to extend this lifetime is to physically separate electrons and holes—for example, by having them reside in different layers of a van der Waals heterostructure. Jauregui *et al.* used this strategy to form long-lived interlayer excitons in a heterostructure made out of monolayers of molybdenum diselenide ($MoSe_2$) and tungsten diselenide (WSe_2). Through electrical control of the layers in the heterostructure, the researchers further increased exciton lifetime and formed and manipulated charged excitons.

Science, this issue p. 870